

Oriented Boxes for Accurate Instance Segmentation

Patrick Follmann 

Research
MVTec Software GmbH
Munich, Germany

Rebecca König 

Research
MVTec Software GmbH
Munich, Germany

Abstract—State-of-the-art instance-aware semantic segmentation algorithms use axis-aligned bounding boxes as an intermediate processing step to infer the final instance mask output. This often leads to coarse and inaccurate mask proposals due to the following reasons: Axis-aligned boxes have a high background to foreground pixel-ratio, there is a strong variation of mask targets with respect to the underlying box, and neighboring instances frequently reach into the axis-aligned bounding box of the instance mask of interest.

In this work, we overcome these problems by proposing to use oriented boxes as the basis to infer instance masks. We show that oriented instance segmentation improves the mask predictions, especially when objects are diagonally aligned, touching, or overlapping each other. We evaluate our model on the D2S and Screws datasets and show that we can significantly improve the mask accuracy by 10% and 12% mAP compared to instance segmentation using axis-aligned bounding boxes, respectively. On the newly introduced Pill Bags dataset we outperform the baseline using only 10% of the mask annotations.

Index Terms—instance segmentation, oriented box detection

I. INTRODUCTION

The precise localization of objects in natural images is fundamental for many industrial tasks, such as bin-picking or object counting. The detection is often done using axis-aligned boxes [18], [24]. However, if objects are deformable, articulated, or diagonally oriented, axis-aligned bounding boxes are often only a very coarse approximation of the objects' locations. Instance-aware semantic segmentation (instance segmentation), as introduced in [19], tries to overcome this limitation by predicting a pixel-precise mask for each of the instances. However, recent instance segmentation methods that are at the top of instance segmentation challenge leaderboards, such as FCIS [16] or variants of Mask RCNN [9], rely on axis-aligned box proposals to infer the instance mask per box.

This intermediate axis-aligned box detection step introduces several limitations to the final instance mask output:

Depending on an object's orientation, a majority of the box covers the background or another instance that is not of interest for the mask prediction. As features are pooled with respect to the box, this can lead to false classifications or mask predictions reaching into neighboring objects as shown in Fig. 1. Overlapping bounding boxes also increase the likelihood that one of the candidate boxes is mistakenly filtered out by non-maximum-suppression (NMS).

If an object is rotated, the bounding box aspect-ratio can vary significantly. For unsymmetric objects this leads to highly varying mask targets with respect to the bounding box, even

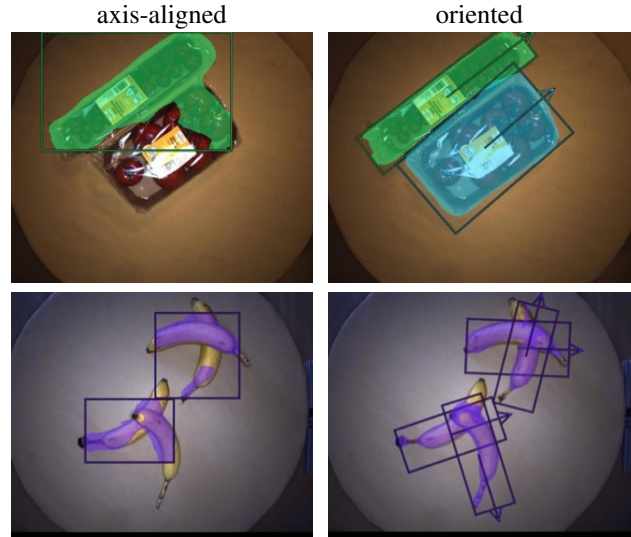


Fig. 1: **Benefits of oriented instance segmentation.** Qualitative comparison of our proposed method based on oriented boxes and the baseline based on axis-aligned boxes. Oriented boxes contain fewer background pixels and avoid reaching into neighboring instances. Resulting instance masks are much more accurate.

for very precise box predictions which are generally not given. As a consequence, more pixel-wise annotated instances are necessary to learn these variations.

For large and diagonally oriented instances, the relatively coarse resolution often used for mask prediction can lead to inaccurate mask boundaries because of interpolation artifacts. The use of finer grids can resolve this issue to some extent, but comes at the cost of higher computation time and memory consumption.

Therefore, in this work we propose using oriented as opposed to axis-aligned bounding boxes to infer instance masks. The best possible intersection over union (IoU) an oriented bounding box can achieve for an arbitrary mask is typically much higher than the IoU of the axis-aligned bounding box [2]. Moreover, the oriented instance segmentation (OIS) solves the aforementioned issues of axis-aligned instance segmentation (AAIS):

- Independent of an object's orientation, most of the bounding box area overlaps with the instance of interest. This increases the mask-to-background ratio for mask targets and avoids large overlaps with neighboring objects.

- Bounding box aspect ratios become invariant to an object’s rotation and the mask exhibits significantly smaller variations with respect to the pooling grid. This leads to more consistent mask targets and a better conditioned training.
- For objects with non-overlapping masks, oriented bounding boxes overlap significantly less than axis-aligned bounding boxes. This prevents false positive mask predictions within neighboring objects.
- Especially for large, elongated and diagonally aligned objects the accuracy of mask predictions at their boundaries is increased because long edges are aligned with the oriented box.

The main contributions of this paper are: We propose to predict accurate instance masks based on oriented box detections. Our approach can be easily applied to existing models based on axis-aligned boxes to enhance their performance. We describe how to adapt architectures for *OIS* and explain necessary changes to different parts of the model compared to baseline *AAIS* models. Our evaluation on three datasets *D2S* [6], *Screws* [25] and the newly introduced *Pill Bags* dataset shows that the mask accuracy is improved significantly. This leads to a strong increase in overall mAP from 45% to 55% on *D2S* with a Mask RCNN architecture [9] and from 46% to 55% with a RetinaMask architecture [8]. On *Screws* the overall mAP is improved from 41% to 53%. Moreover, we show that on *Screws* the predicted mask output of our model can be directly used to further refine the oriented box output and improve the box mAP by 1.5%. Further, we show on *Pill Bags* that for *OIS* only 10% of the mask annotations are required to outperform the *AAIS* baseline.

II. RELATED WORK

a) Instance segmentation.: To date, most instance segmentation methods are based on a Faster RCNN [24] two-stage object detector. The first stage, *i.e.* the region proposal network (RPN) stage, proposes axis-aligned class-agnostic boxes at all locations where an object is likely to be found. The second stage pools box-specific features with a region of interest (RoI) pooling and refines them to classify the proposals into one of the target classes or background. A second, parallel branch (sometimes with shared weights) is used to further improve the box coordinates via bounding-box regression. In Mask RCNN, He *et al.* [9] propose to pool features once again, typically with a grid size of 14×14 , for a third parallel branch that predicts the instance mask. The architecture of the mask prediction branch is similar to the decoder of a fully convolutional network for semantic segmentation [22]. It consists of a number of intermediate convolutions before a transposed convolution upsamples the features by a factor of 2 in each spatial dimension and finally mask probabilities are predicted using a sigmoid activation. PA-Net [21] optimizes the information flow within Mask RCNN by fusing the features of several feature pyramid network (FPN) [17] levels to improve the quality, but at the cost of runtime. Mask Scoring RCNN [11] learns to predict the quality of the mask predictions, which

improves the mAP by recalibrating the predicted scores such that low quality masks also receive a lower score compared to higher quality masks. Among the more recent methods, YOLACT [1] improves the speed of instance segmentation by using a linear combination of prototypes for mask prediction and a fast variant of non-maximum-suppression. Shape priors are also used in ShapeMask [14], mainly with the goal to improve the generalizability of the model and to reduce the amount of necessary annotated training data. RetinaMask [8] extends the single-stage box detector RetinaNet [18] to instance segmentation by adding a mask branch similar to Mask RCNN. In contrast to our method, all of the existing instance segmentation methods rely on axis-aligned bounding boxes.

b) Oriented box detection.: The idea of oriented box detection has been introduced in the context of scene text detection. Existing methods are all based on Faster RCNN [24]. Jiang *et al.* [13] still use an axis-aligned box RPN but infer an oriented final box output by regressing the orientation. In [23], Ma *et al.* extend the RPN to use oriented anchors and the RoI pooling to pool features with respect to oriented boxes. Oriented box detection has been demonstrated to perform well on other domains than in OCR. For example, Ding *et al.* [5] have set a new benchmark on the oriented object detection dataset DOTA [26]. In contrast to our work and [23], they do not use oriented anchors but propose a RoI Transformer module before pooling with respect to the oriented box. Another application that benefits from the use of oriented boxes is ship detection in satellite images [27], where the authors propose a dense FPN with oriented anchors.

c) Oriented instance segmentation.: To the best of our knowledge, we are the first to combine the approach of *AAIS* methods with oriented box detection to increase the instance mask accuracy. We exemplarily extend the *AAIS* architectures RetinaMask [8] and Mask RCNN [9] to *OIS*.

III. ORIENTED INSTANCE SEGMENTATION

In the following, we present the key components to make the simple idea of *OIS* work efficiently. Our approach is applicable to all *AAIS* methods. An exemplary *OIS* architecture based on Mask RCNN [9] is depicted in Fig. 2: In a first step, the backbone is applied to the input image to extract features that are used for the three following stages: The first stage is the RPN, which predicts for each of a number of template *anchor boxes* whether it is likely that an object with similar bounding box is present or not (fg/bg branch) and if so, how the anchor should be refined to better match the underlying object (box branch). The second stage are the RCNN heads, where the oriented box proposal outputs of the RPN are used to RoI pool the features for class prediction (class branch) and further box refinement (box branch). The third stage uses the final RCNN head oriented box output to again RoI pool the features to feed the mask prediction head that outputs a pixel-precise mask for each of the final boxes. All RoI pooling layers pool from the oriented grid aligned with the input boxes. Since the output

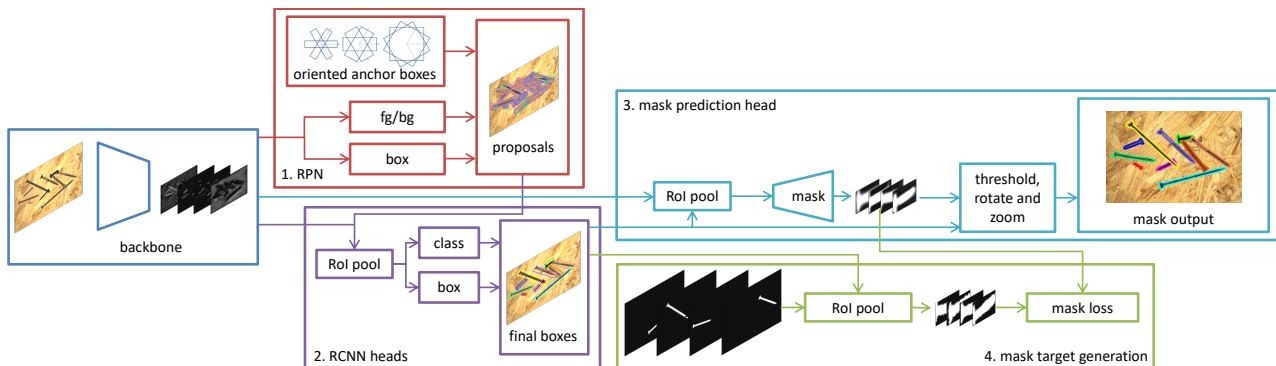


Fig. 2: **Exemplary OIS Architecture.** (blue, center left): Input image and backbone for feature extraction. (red, top): Oriented RPN. (violet, bottom): Features are pooled with respect to oriented proposals to feed RCNN heads for final oriented box output. (cyan, middle): Features are pooled with respect to final boxes to feed the branch for mask prediction. Finally, mask probabilities are fit to the oriented box output and thresholded. (green, bottom-right): During training, mask targets are calculated by RoI pooling the GT masks.

feature maps are upright, usual convolutions can be used in the subsequent layers.

For an *OIS* version of RetinaMask [8] the same strategy can be applied. The only difference is that the RCNN heads of the second stage are fused with the RPN stage that directly outputs class probabilities and the final boxes.

a) *Box representation.*: We use a five parameter representation for boxes $b = (r, c, l1, l2, \phi)$, where (r, c) denote the subpixel-precise center point row and column coordinates, $(l1, l2)$ the semi-axes lengths of the oriented box, and ϕ the orientation pointing in the direction of the major axis. ϕ is given as an angle in radians between the positive horizontal axis and the $l1$ -axis in mathematically positive sense. In contrast to the parametrization used in [23], we do not enforce that $l1 \geq l2$ such that sudden flips of the orientation for boxes with aspect ratio close to one are avoided.

b) *RPN.*: Because we want to predict oriented boxes, the region proposal network is fed with oriented anchors with different orientations, aspect ratios, and subscales. Ding *et al.* [5] argue that this leads to a massively higher number of anchors compared to axis-aligned boxes. However, we choose the orientation of the ground truth (GT) boxes such that it is aligned with the longer box side-length. Therefore, only aspect ratios smaller or equal to one are necessary, which almost halves the number of anchors.

As usual, the anchor target assignment is based on the IoU between anchors and GT: If an anchor has an IoU higher than $fgPosThresh$ with a GT box it is assigned to the foreground and if the IoU is lower than $fgNegThresh$ it is assigned to the background. If the IoU is between $fgNegThresh$ and $fgPosThresh$ and there is another anchor that has a higher IoU with this GT, the anchor is ignored. However, if the IoU is higher than $fgNegThresh$ and it is the highest IoU that was achieved by any anchor for this GT box, the anchor is assigned to foreground.

With a naive implementation we noticed that for *OIS* the training is very unstable or converging to a bad local minimum due to the following reasons: On the one hand, the number of foreground anchors is very low or in some cases there is not

a single anchor assigned to a particular GT instance. On the other hand, the exact oriented box IoU sometimes leads to very inefficient assignments (cf. Fig. 3b). To fix the latter, we replace the exact IoU by the angle-related IoU (arIoU [20]) for anchor assignment:

$$\text{arIoU}(A, B) = \max(0, \cos(\phi_A - \phi_B)) \cdot \text{IoU}(\hat{A}, B), \quad (1)$$

where \hat{A} is the box $(r_A, c_A, l1_A, l2_A, \phi_B)$.

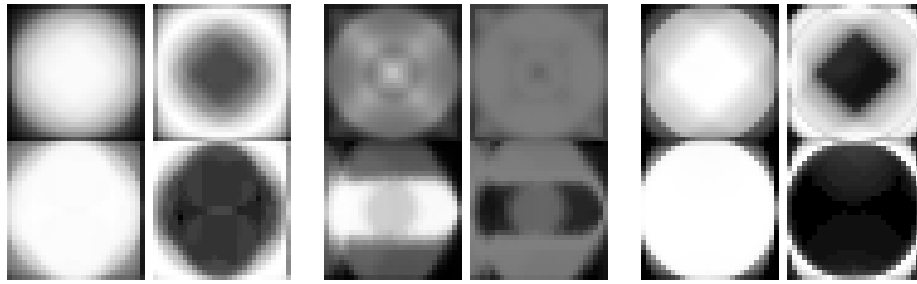
Although the arIoU can fix the problem of wrong anchor assignment, the second problem of a low number of foreground instances remains because its values can still become small for anchors that have only slightly different parameters than the GT box. To fix this problem and increase the number of foreground anchors we decrease $fgNegThresh$. Moreover, we evaluate the influence of *setting weak boxes to background* ($swb2bg$): If $swb2bg$ is set to *false*, anchors that achieve the highest arIoU with a GT box, but where the arIoU is below $fgNegThresh$ are still assigned to the foreground. By changing $fgNegThresh$ and $swb2bg$ we assure that all GT instances contribute to the training, although none of the anchors fits perfectly. Hence, instead of increasing the number of anchors, these changes offer an efficient way to address all available GT box shapes. Effectively, this leads to a more stable training because enough foreground examples are present.

The relaxation of $fgNegThresh$ and $swb2bg$ are only used in the RPN. For the RCNN heads and the mask head, we only want good box proposals to contribute to the training. This is in line with the findings of [3], where the assignment thresholds are increased in several iterative box refinements.

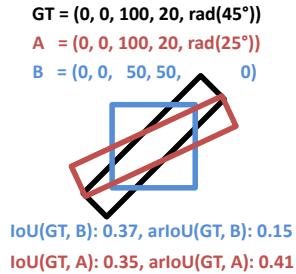
c) *Oriented box targets.*: We use the following box target calculations for the row and column coordinate deltas:

$$d_r = \frac{r^* - r}{\bar{l}}, \quad d_c = \frac{c^* - c}{\bar{l}}, \quad (2)$$

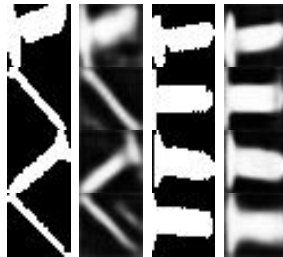
where (r^*, c^*) are coordinates of the GT box, (r, c) are coordinates, and $\bar{l} = (l1 + l2)/2$ is the mean axis length of the box for which the deltas should be calculated. Using \bar{l} for normalization there is no dependency on the orientation of the box. In previous work, such as [5], [23], $l2$ is used to



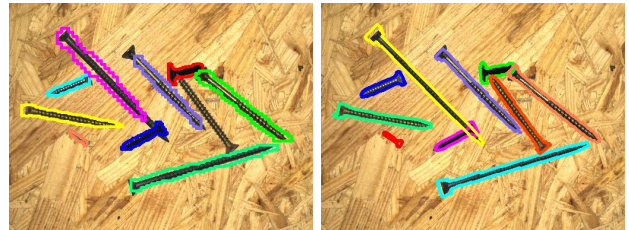
(a) Mean and deviation of GT masks for *D2S*, *Screws* and *Pill Bags* (left to right), (top) *AAIS*, (bottom) *OIS*



(b) arIoU



(c) Mask targets



(d) Outputs: (left) *AAIS*, (right) *OIS*

Fig. 3: Mean and deviation of GT masks, arIoU & comparison of mask targets and results. (a) The mean and standard deviation of the first 3000 instance masks that are pooled to a size of 28×28 with respect to the GT boxes. (b) arIoU example: (black) GT box, (red, blue) oriented anchors. Although, for the blue anchor the coordinates $l1, l2$, and ϕ differ a lot, the exact IoU is higher than for the red anchor where only ϕ differs by 20° . This issue is solved by the use of the arIoU for anchor assignment. (c) randomly chosen mask targets and mask probabilities, in the left two columns for *AAIS*, in the right two columns for *OIS*, respectively. (d) Final mask output for *AAIS* and *OIS* on a generated *Screws* image (left and right)

normalize d_r and $l1$ to normalize d_c instead of the mean value \bar{l} . However, if a box is oriented with $\phi \geq \frac{\pi}{2}$ the connotation of $l1$ and $l2$ with respect to r and c is flipped. This is avoided by the use of \bar{l} .

Moreover, in the calculation of the target delta for the orientation d_ϕ , we avoid large regression targets by ensuring that d_ϕ is in the range $(-\frac{\pi}{2}, \frac{\pi}{2})$ due to the use of the arIoU during the assignment phase.

d) Oriented mask prediction.: For each predicted oriented box, features are pooled with an oriented RoI-pooling layer, such that the batch size of the mask branch equals the input batch size times the maximal number of predictions. The pooled feature maps with $m \times m = 14 \times 14$ spatial dimension are fed into a sequence of n convolutions with ReLU activation followed by an upsampling transposed convolution. Finally, a sigmoid activation is applied to get the mask probability of each pixel within the warped box. Mask prediction is done class-agnostically since it has already been shown in [9] that a class-specific mask prediction does not improve the results significantly but comes at a higher computational cost.

For target generation, the GT masks are painted into a multi-channel binary image, where each channel contains the GT mask of one instance. Given the final box predictions, the assignment to the GT instances is done in the same way as in the RPN based on the arIoU. In this separate assignment step, we increase both IoU thresholds such that only good final boxes contribute to the training of the mask branch. If a final

box is not assigned to any GT instance, the corresponding weights in the mask prediction loss are set to zero such that the predicted mask is ignored. We use a modified, oriented RoI-pooling on the multi-channel GT mask image that only pools within the channel indices of the assigned GT masks to obtain the mask probability targets for the predicted boxes (cf. bottom-right of Fig. 2). A sigmoid cross-entropy loss is used to train the mask branch.

As in [9], a final grid size of 28×28 pixels for mask targets and prediction is used. This low resolution limits the detailedness of the output masks. However, as the oriented boxes generally contain much less background than the axis-aligned boxes, the given resolution is used much more efficiently. This is visualized in Fig. 3a and Fig. 3c, where for *OIS* the targets' and predictions' variance between different instances is significantly lower than for *AAIS*. On the one hand, *OIS* models can learn a stronger prior for the mask prediction since especially in the middle of the object it is very likely that the object is present. The capacity of the model can be focused on the boundary of the instances, where they differ the most. On the other hand, the mask prediction is done based on a higher resolution relative to the instance size. This gives the model more flexibility to capture fine details of the instance shape.

During inference, to obtain the final mask, the mask probabilities are thresholded by 0.5 and the obtained region is rotated, translated and zoomed according to the corresponding

predicted box.

e) Classes without orientation.: In many applications, not only objects with a clearly defined orientation are of interest. If we use the smallest oriented bounding box as GT for symmetric or round objects, the orientation is varying between different instances without a hint for the model why this is the case. This can lead to a destabilization of the training. Therefore, we propose to assign these classes to a group of *classes without orientation*.

For these categories, we annotate the GT boxes as the smallest axis-aligned bounding boxes of the GT instance masks with $\phi = 0$.

f) Implementation Details.: We differentiate between two scenarios: The first scenario is that we are interested in the exact orientation of boxes, i.e., $\phi \in (-\pi, \pi]$. In the second scenario, ϕ is limited to the range $(-\frac{\pi}{2}, \frac{\pi}{2}]$, which is suitable if the actual orientation of the box is not important, but only a tight oriented bounding box of the instance mask is the goal. In this case, predictions with ϕ outside of the range can be corrected by subtracting or adding π . To differentiate the two scenarios, we use a parameter *IgnoreDirection* that is set to *true* in the latter case. Note that it is important that also the GT given in the dataset at hand is annotated in accordance to *IgnoreDirection*.

Box-based instance segmentation models can be easily modified to be trainable only with mask GT available for a fraction of the training instances: Whenever the mask GT is not available for an instance, we set the loss weights of this instance within the mask branch to zero. Therefore, the prediction for this instance will be ignored during the loss computation.

IV. EXPERIMENTS

In the following subsections, we evaluate our *OIS* model on three different datasets: namely the *D2S* [6], *Screws* [25] and the newly introduced *Pill Bags* dataset. All datasets have high-quality annotations such that a potentially improved mask accuracy can be measured.

To measure the potential benefit of *OIS* compared to *AAIS*, we compute the IoU of the GT mask with both the smallest oriented and axis-aligned bounding box for each instance. The mean box mask IoU shown in Table I contains the mean IoU values averaged over all classes. It shows how tighter the oriented boxes are on average. For all three datasets, the difference is significant and in the following we show that this potential can indeed be utilized.

dataset	axis-aligned	oriented
<i>D2S</i>	62%	81%
<i>Screws</i>	46%	58%
<i>Pill Bags</i>	73%	84%

TABLE I: **Mean box mask IoU.** Mean IoU of smallest bounding box with mask computed for each instance of a class and averaged over all classes. For all three datasets, oriented bounding boxes approximate the mask a lot better than axis-aligned bounding boxes

A. *D2S*

The densely segmented supermarket dataset (*D2S*) [6] contains 60 different categories of supermarket products lying on a turntable and captured in a top-down view with various orientations. There are elongated objects such as lying bottles, boxes, certain vegetables like carrot, or zucchini, but also round or highly deformable objects such as standing bottles, apples, or nets filled with oranges.

Because the instances are touching or overlapping in many cases, the dataset is very challenging. Moreover, difficult scenes are only contained in the validation and test splits, which requires data augmentation to enhance the training set.

In *D2S*, each image is captured with three different lightings (normal, bright, and dark), but our focus is to show that *OIS* improves the mask quality compared to the *AAIS* baseline. Hence, we only use the normal lighting images. Further, we scale the images to a relatively low resolution of 512×384 to speed up the training and evaluation.

a) Data preparation and model settings.: To have a fair comparison, we use exactly the same training data for all models. As mentioned, for *D2S* it is necessary to generate additional training data by utilizing the existing annotations of the training set. We follow the approach of [7] and crop random instances from the training set using their ground truth masks before pasting them onto random backgrounds that look similar to the ones of the validation and test set. 2000 additional augmented training images are generated with random backgrounds and randomly positioned and rotated instances. The dataset consists of 9000 images in total: 2000 augmented images plus 1960 original training images, 1200 validation images and 4340 test images. Examples for generated images are given in the supplementary material. For *D2S*, we assign the following classes to *classes without orientation*: *apple_golden_delicious*, *apple_granny_smith*, *apple_red_boskoop*, *clementine*, *clementine_single*, *orange_single*, *oranges*, *lettuce*, *salad_iceberg*. By their nature, these categories have no well-defined orientation. We set *IgnoreDirection* to *true* for *D2S* experiments.

For the training, validation, and test splits, the box ground truth for *OIS* is generated as follows: We use the smallest oriented bounding box of the instance mask by default, except for *classes without orientation*, where the smallest axis-aligned bounding box is used.

For both RetinaMask (R) and Mask RCNN (M), we use the same network architecture for *AAIS* and *OIS*. For *AAIS*, we replace oriented anchors with axis-aligned anchors and use the default axis-aligned RoI pooling operations. All other model hyperparameters are the same as for *OIS*. In the RetinaMask experiments, we use two aspect ratios and three orientations for *OIS* and six aspect ratios for *AAIS* to get the same number of anchors. Interestingly the result could not be improved using more aspect ratios in the *OIS* case. As backbone we use a ResNet-50 [10] pretrained on ImageNet [4]. Note that we train all other weights of the RPN, the RCNN, and mask heads from scratch. We train the models for 50 (M) and 40 (R) epochs and evaluate after each epoch on the validation set

model	AABB	OBB	mask	mask agn
AAIS (M)	51%	9%*	45%	49%
OIS (M)	52%*	48%	55%	61%
AAIS (R)	54%	8%*	46%	55%
OIS (R)	54%*	50%	55%	65%

TABLE II: **D2S results.** mAP values on the test set. AABB: axis-aligned box, OBB: oriented box, mask: instance mask, mask agn: same as mask, but without evaluating the class prediction. *OIS* clearly improves the mask mAP. (*) boxes are calculated from mask predictions

$\neg swb2bg$	$fgNegThresh$	cwo	OBB	mask
			31.56% \pm 0.004	40.13% \pm 0.002
✓			32.58% \pm 0.004	40.85% \pm 0.001
✓	✓		44.84% \pm 0.001	53.39% \pm 0.001
✓	✓	✓	47.01% \pm 0.012	54.06% \pm 0.008

TABLE III: **Ablation study for D2S.** mean Mask mAP values on test set over three independent runs and their standard deviation. Increasing the number of foreground examples in training by decreasing $fgNegThresh$ and disabling $swb2bg$ improves the results. Setting cwo additionally improves the mask mAP

(using box mAP). The results are always shown for the best model regarding the validation set mAP (early stopping) over 3 (M) and 1 (R) independent runs. All other training and model parameters can be found in the appendix.

b) Analysis.: Fig. 5 shows qualitative results on *D2S* test images. In comparison to *AAIS*, the *OIS* mask predictions are much more accurate, especially for diagonally oriented objects. Due to the less precise mask targets in *AAIS*, also the mask probabilities become inexact. In combination with the upscaling to the final box size and thresholding, the mask output is often not exactly in correspondence with the instance boundaries. In case of overlapping or touching objects, *OIS* clearly shows better results as in those cases the box overlap is lower. In many cases for *AAIS*, the mask is extended into the background or onto neighboring objects.

Generally, if the box is predicted correctly, the mask is very precise for *OIS*. This is a clear improvement to *AAIS* consistently across *RetinaMask* and *Mask RCNN*, which also reflects in mAP-values shown in Table II. Fig. 4 shows that especially for high IoU-thresholds, the mAP can be significantly improved by *OIS*: E.g., from 50% to 65% @IoU0.75 and from 21% to 41% @IoU0.85.

Since *AAIS* predicts axis-aligned boxes, we can only evaluate the box mAP for the axis-aligned ground truth boxes. Interestingly, if we use the axis-aligned smallest bounding boxes of the instance masks predicted by *OIS* (M), the mAP of 55% outperforms the box mAP of *AAIS* (M). In contrast, calculating the oriented box from the *AAIS* mask does not work at all. Moreover, in contrast to *AAIS*, for *OIS* the mask mAP is even higher than the oriented box mAP, which shows that the mask prediction is very precise. Since our focus is to improve mask accuracy, we also show results where the predicted class is not taken into account (class-agnostic evaluation). Also in this case, the mask mAP can be improved substantially.

c) Ablation study.: We also perform an ablation study for *OIS* to empirically confirm our hyperparameter settings.

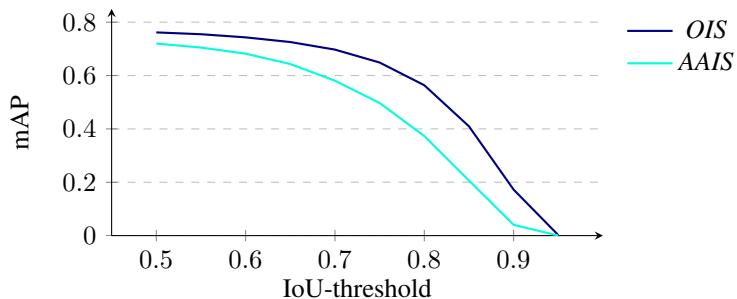


Fig. 4: **Mask RCNN on D2S.** Mask mAP-values for IoU-thresholds from 0.5 to 0.95. Consistently and especially for high IoU-thresholds *OIS* improves the mAP significantly

Results are shown in Table III. Namely, we evaluate the influence of reducing $fgNegThresh$ from 0.4 to 0.3 and switching off $setWeakBoxesToBg$ ($swb2bg$), as well as using *classes without orientation* (cwo). The results indicate that $swb2bg$ and cwo only slightly improve the mask mAP and the most benefit comes from reducing $fgNegThresh$. Using cwo mainly improves the box mAP because this assures that for symmetric or round objects the orientation of the bounding box is well defined. Overall, the mask mAP can be drastically improved from 40% to 54%.

B. Screws

The *Screws* [25] dataset contains 9 different types of screws and 4 different types of nuts on a wooden background. The categories differ in size, length, and color, but some are only distinguishable by a different thread. Typical example images are shown in Fig. 8.

The dataset consists of 384 images, of which 70% belong to the train set, 15% to the validation set, and 15% to the test set. Ground truth annotations are given as oriented boxes. As the nut-classes are symmetric and the orientation is not well-defined, these four classes are assigned to *classes without orientation*. In this dataset for screw classes, the exact orientation pointing from the screws head to its tail is of interest. Therefore, $IgnoreDirection$ is set to *false* such that box orientations are in the range $(-\pi, \pi]$.

a) Generated training data.: Because the pixel-precise annotation of instance masks is tedious and time-consuming, we follow the approach of [25] to generate artificial training images. Therefore, each category is captured on a homogeneous white background where a relatively precise instance mask can be obtained by thresholding. In this weakly-supervised setting, we use a single template image per category and generate 800 images (350 train, 150 validation, 300 test) by cropping and pasting random instances onto empty wooden backgrounds similar to those of the original dataset. A generated example image is shown in Fig. 3.

To train and evaluate *AAIS*, we obtain the box ground truth annotations as the smallest axis-aligned bounding box of instance masks. The oriented box ground truth for categories with orientation is generated as follows: The orientation of the

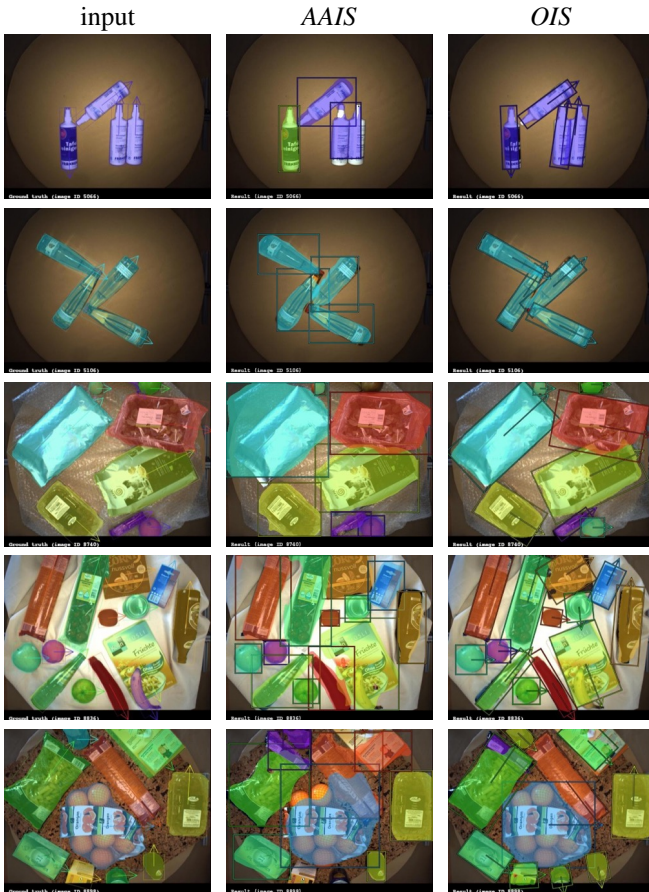


Fig. 5: *D2S* results. (from left to right) input image with ground truth masks and generated ground truth oriented boxes, results of *AAIS*, results of *OIS*. *OIS* clearly improves the mask accuracy, especially for close-packed, elongated, and diagonally oriented objects. More results can be found in the supplementary material (best viewed digitally with zoom)

box is calculated based on the second moments of the instance mask (cf. appendix). To get the orientation pointing from the screws head to its tail, the orientation is corrected by adding or subtracting π if the orientation from the center of gravity to the most distant point on the mask boundary is pointing into the opposite direction.

b) *Model settings*.: We train all models only on the generated training set. Because *Screws* has less intra-class variations and less variations due to changes in perspective, the dataset is less complex than *D2S*. Therefore, in *Screws* experiments we use a SqueezeNet [12] backbone, which speeds up the training process. This also shows that the proposed *OIS* model is superior independent of the backbone or other hyperparameters shown in the appendix.

c) *Evaluation on generated data*.: Quantitative results are shown in Table 6: First, we evaluate *AAIS* and *OIS* on the generated test set, where the box mAP is very similar for *AAIS* and *OIS* (55.2% vs. 58.7%). Also here, the clear improvement of mask mAP (41.5% *AAIS* to 53.4% *OIS*) shows that the masks can be predicted much more precise for *OIS*.

model	AABB	OBB	mask
<i>generated data</i>			
<i>AAIS</i>	55.2%	-	41.5%
<i>OIS</i>	-	58.7%	53.4%
<i>real data</i>			
<i>AAIS bfm</i>	-	36.1%	-
<i>OIS bfm</i>	-	45.6%	-
<i>OIS</i>	-	51.4%	-
<i>OIS ofm</i>	-	52.9%	-

TABLE III: *Screws Mask RCNN* results. mAP values on the test sets. AABB: axis-aligned box result, OBB: oriented box result, mask: instance mask result. *OIS* clearly improves the mask mAP and the generated masks are a lot more consistent with the instances

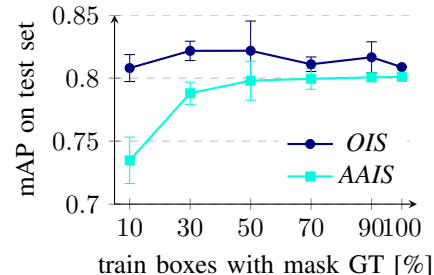


Fig. 7: *Pill bags* partial supervision. For *OIS*, if only 10% of the boxes contain a mask ground truth, the mAP is on the same level as with all mask annotations. *AAIS* needs at least 50% of the boxes labeled with instance masks

d) *Evaluation on real data*.: Because the original *Screws* dataset only contains oriented box annotations, we predict instance masks and use them to calculate oriented boxes in the same way as was done for the ground truth of the generated dataset (box from mask *bfm*). By this, we measure how well the predicted masks are aligned with the instance. For *OIS*, we can also evaluate the predicted oriented boxes. The result of *OIS ofm* is using the predicted box from *OIS*, where ϕ is changed to the orientation calculated from the predicted mask.

Table 6 shows that for *AAIS* the predicted masks do not coincide with the instances, as the box mAP of 36.1% is rather low. For *OIS*, this result is increased by a large margin to 45.6%. The result is still slightly below the box result directly predicted from *OIS*. However, if predicted masks are used to refine the orientation as in *OIS ofm* the box results can be further improved by 1.5%. Qualitative results are shown in Fig. 8.

C. Pill Bags

The *Pill Bags* dataset contains 398 images of 10 different pill categories captured within a plastic bag. Overall the dataset contains 4048 instances, whereof 2826, 622, and 600 belong to the 278, 61, and 59 images of the training, validation and test sets, respectively. As in a typical industrial application, all images have more or less the same appearance. Moreover, the pills have not many deformations and their shape is close to that of an ellipse. Therefore, it is not surprising that the

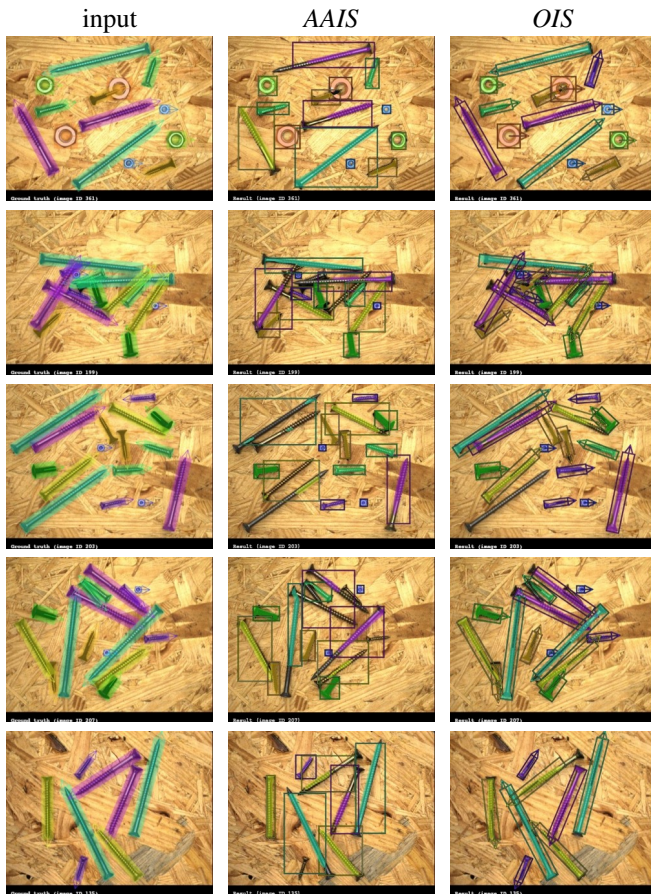


Fig. 8: **Screws results.** (from left to right) real input with ground truth boxes, results of AAIS, results of OIS. Models were trained only on generated data. OIS clearly improves the mask accuracy, especially for close-packed, elongated, and diagonally oriented objects. More results can be found in the supplementary material (best viewed digitally with zoom)

instance segmentation task can already be solved quite well with AAIS. However, in our experiments on *Pill Bags*, we analyze how many of the instance mask labels are necessary to obtain a good result. Therefore, we delete all but a fraction of the annotated GT instance masks and whenever the mask is not available during training, we set the corresponding mask loss weight of this instance to zero. This allows to train only with a fraction of the expensive instance mask labels, which are tedious to annotate.

Fig. 7 shows that for OIS we can already successfully train instance segmentation if only 10% of the masks are annotated in the training set - without a significant reduction in mask mAP on the test set. In comparison, the AAIS method significantly benefits from more annotations. Even using all annotations the AAIS resulting mAP is lower than the 10% counterpart of OIS. This can be explained by the higher variance of the mask within the axis-aligned bounding boxes. Interestingly, for both methods the best results can be obtained when only a fraction of the instances are annotated. Some

qualitative examples are shown in Fig. 9.

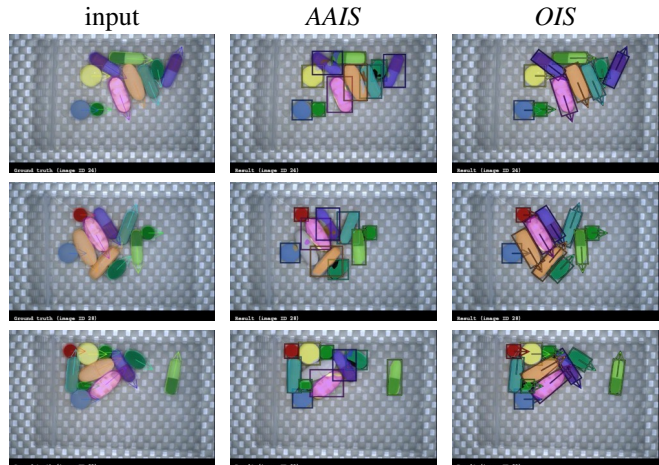


Fig. 9: **Pill Bags results.** (from left to right) input image with GT masks and GT oriented boxes, results of AAIS (R), results of OIS (R). Both models have been trained with only 10% of GT instance masks available.

V. CONCLUSION

In this work, we have presented an instance segmentation model that predicts instance masks based on oriented box predictions. The use of oriented boxes leads to a more precise approximation of the instance masks and results in very accurate mask predictions. We have shown that the overall mask mAP on *D2S* and *Screws* can be improved significantly. The predicted instance masks are very accurate, such that they can be used to improve the axis-aligned box detection on *D2S* and the oriented box detection on *Screws*. Moreover, oriented instance segmentation on *Pill bags* requires only 10% of instance mask annotations.

REFERENCES

- [1] Daniel Bolya, Chong Zhou, Fanyi Xiao, and Yong Jae Lee. Yolact: real-time instance segmentation. In *Proceedings of the IEEE International Conference on Computer Vision*, pages 9157–9166, 2019. 2
- [2] Tobias Böttger, Patrick Follmann, and Michael Fauser. Measuring the accuracy of object detectors and trackers. In *German Conference on Pattern Recognition*, pages 415–426. Springer, 2017. 1
- [3] Zhaowei Cai and Nuno Vasconcelos. Cascade R-CNN: Delving into high quality object detection. In *Proceedings of the IEEE conference on computer vision and pattern recognition*, pages 6154–6162, 2018. 3
- [4] Jia Deng, Wei Dong, Richard Socher, Li-Jia Li, Kai Li, and Li Fei-Fei. ImageNet: A large-scale hierarchical image database. In *CVPR*, pages 248–255, 2009. 5, 17
- [5] Jian Ding, Nan Xue, Yang Long, Gui-Song Xia, and Qikai Lu. Learning RoI transformer for oriented object detection in aerial images. In *Proceedings of the IEEE Conference on Computer Vision and Pattern Recognition*, pages 2849–2858, 2019. 2, 3
- [6] Patrick Follmann, Tobias Böttger, Philipp Härtinger, Rebecca König, and Markus Ulrich. MVTec D2S: Densely Segmented Supermarket Dataset. In Vittorio Ferrari, Martial Hebert, Cristian Sminchisescu, and Yair Weiss, editors, *Computer Vision – ECCV 2018*, pages 581–597, Cham, 2018. Springer International Publishing. 2, 5
- [7] Patrick Follmann, Bertram Drost, and Tobias Böttger. Acquire, augment, segment and enjoy: Weakly supervised instance segmentation of supermarket products. In Thomas Brox, Andrés Bruhn, and Mario Fritz, editors, *Pattern Recognition*, pages 363–376, Cham, 2019. Springer International Publishing. 5

- [8] Cheng-Yang Fu, Mykhailo Shvets, and Alexander C Berg. Retinamask: Learning to predict masks improves state-of-the-art single-shot detection for free. *arXiv preprint arXiv:1901.03353*, 2019. [2](#), [3](#), [10](#), [16](#)
- [9] Kaiming He, Georgia Gkioxari, Piotr Dollar, and Ross Girshick. Mask R-CNN. In *ICCV*, pages 1059–1067, 2017. [1](#), [2](#), [4](#), [10](#), [16](#)
- [10] Kaiming He, Xiangyu Zhang, Shaoqing Ren, and Jian Sun. Deep residual learning for image recognition. In *Proceedings of the IEEE conference on computer vision and pattern recognition*, pages 770–778, 2016. [5](#), [17](#)
- [11] Zhaojin Huang, Lichao Huang, Yongchao Gong, Chang Huang, and Xinggang Wang. Mask scoring R-CNN. In *Proceedings of the IEEE Conference on Computer Vision and Pattern Recognition*, pages 6409–6418, 2019. [2](#)
- [12] Forrest N Iandola, Song Han, Matthew W Moskewicz, Khalid Ashraf, William J Dally, and Kurt Keutzer. Squeezenet: Alexnet-level accuracy with 50x fewer parameters and < 0.5 mb model size. *arXiv preprint arXiv:1602.07360*, 2016. [7](#), [10](#), [15](#)
- [13] Yingying Jiang, Xiangyu Zhu, Xiaobing Wang, Shuli Yang, Wei Li, Hua Wang, Pei Fu, and Zhenbo Luo. R2CNN: Rotational region CNN for orientation robust scene text detection. *arXiv preprint arXiv:1706.09579*, 2017. [2](#)
- [14] Weicheng Kuo, Anelia Angelova, Jitendra Malik, and Tsung-Yi Lin. Shapemask: Learning to segment novel objects by refining shape priors. *arXiv preprint arXiv:1904.03239*, 2019. [2](#)
- [15] Alina Kuznetsova, Hassan Rom, Neil Alldrin, Jasper Uijlings, Ivan Krasin, Jordi Pont-Tuset, Shahab Kamali, Stefan Popov, Matteo Mallocci, Tom Duerig, and Vittorio Ferrari. The open images dataset v4: Unified image classification, object detection, and visual relationship detection at scale. *arXiv:1811.00982*, 2018. [10](#), [15](#)
- [16] Yi Li, Haozhi Qi, Jifeng Da, Xiangyang Ji, and Yichen Wei. Fully convolutional instance-aware semantic segmentation. In *Proceedings of the IEEE conference on computer vision and pattern recognition*, pages 2359–2367, 2017. [1](#)
- [17] Tsung-Yi Lin, Piotr Dollár, Ross Girshick, Kaiming He, Bharath Hariharan, and Serge Belongie. Feature pyramid networks for object detection. In *Proceedings of the IEEE conference on computer vision and pattern recognition*, 2017. [2](#)
- [18] Tsung-Yi Lin, Priya Goyal, Ross Girshick, Kaiming He, and Piotr Dollár. Focal Loss for Dense Object Detection. In *International conference on computer vision*, 2017. [1](#), [2](#), [10](#)
- [19] Tsung-Yi Lin, Michael Maire, Serge J. Belongie, James Hays, Pietro Perona, Deva Ramanan, Piotr Dollár, and C. Lawrence Zitnick. Microsoft COCO: common objects in context. In *European Conference on Computer Vision*, pages 740–755, 2014. [1](#)
- [20] Lei Liu, Zongxu Pan, and Bin Lei. Learning a rotation invariant detector with rotatable bounding box. *arXiv preprint arXiv:1711.09405*, 2017. [3](#)
- [21] Shu Liu, Lu Qi, Haifang Qin, Jianping Shi, and Jiaya Jia. Path aggregation network for instance segmentation. In *Proceedings of the IEEE Conference on Computer Vision and Pattern Recognition*, pages 8759–8768, 2018. [2](#)
- [22] Jonathan Long, Evan Shelhamer, and Trevor Darrell. Fully convolutional networks for semantic segmentation. In *Proceedings of the IEEE conference on computer vision and pattern recognition*, pages 3431–3440, 2015. [2](#)
- [23] Jianqi Ma, Weiyan Shao, Hao Ye, Li Wang, Hong Wang, Yingbin Zheng, and Xiangyang Xue. Arbitrary-oriented scene text detection via rotation proposals. *IEEE Transactions on Multimedia*, 20(11):3111–3122, 2018. [2](#), [3](#)
- [24] Shaoqing Ren, Kaiming He, Ross B. Girshick, and Jian Sun. Faster R-CNN: Towards real-time object detection with region proposal networks. *IEEE Transactions on Pattern Analysis and Machine Intelligence*, 39(6):62–66, 2017. [1](#), [2](#), [10](#), [18](#)
- [25] Markus Ulrich, Patrick Follmann, and Jan-Hendrik Neudeck. A comparison of shape-based matching with deep-learning-based object detection. *tm-Technisches Messen*, 86(11):685–698, 2019. [2](#), [5](#), [6](#)
- [26] Gui-Song Xia, Xiang Bai, Jian Ding, Zhen Zhu, Serge Belongie, Jiebo Luo, Mihai Datcu, Marcello Pelillo, and Liangpei Zhang. Dota: A large-scale dataset for object detection in aerial images. In *Proceedings of the IEEE Conference on Computer Vision and Pattern Recognition*, pages 3974–3983, 2018. [2](#)
- [27] Xue Yang, Hao Sun, Kun Fu, Jirui Yang, Xian Sun, Menglong Yan, and Zhi Guo. Automatic ship detection in remote sensing images from google earth of complex scenes based on multiscale rotation dense feature pyramid networks. *Remote Sensing*, 10(1):132, 2018. [2](#)

We provide the following supplementary material:

- Per instance evaluations,
- more detailed qualitative results,
- calculation of orientation of a region,
- detailed model configurations,
- detailed solver settings.

In our paper, we show that for *D2S* and *Screws* (generated), we get large relative mask mAP improvements. Because the mAP depends not only on the accuracy of the mask, but also on the class, in this section we evaluate the mean per instance IoU of predicted masks. Therefore, for each ground truth instance, we calculate the maximum IoU with respect to all predicted instances, independent of the predicted class. We further compute the mean IoU, once over all ground truth instances (all), and once only over instances where the achieved maximum IoU is larger than zero (>0). We also compute the number of instances that result as false negatives because the maximum IoU is below 0.75 (NumFNIoU (@0.75)).

Further, we check if the predicted class of the mask that achieves the maximum IoU for a ground truth instance, is correct. We sum these correctly predicted classes over the whole test dataset in order to see how much the mAP improvement depends on the class prediction.

The results are summarized in Table IV. The mean IoU is improved significantly for *OIS* compared to *AAIS* (both all and >0). This results in a lot less false negatives at IoU threshold 0.75. For *Screws*, the number of predictions with correct class is slightly worse for *OIS* than for *AAIS*. This emphasizes that for *Screws* the mAP improvement is coming from more accurate mask predictions. For *D2S*, the number of predictions with correct class is slightly increased by *OIS*, but still on the same level (81.3% *OIS* vs. 79.8% *AAIS*). Hence, also here the mAP improvement is mainly based on more accurate masks.

In this section we show some more qualitative results. Fig. 10 shows further results for *D2S* and Fig. 11 for *Screws* (generated), respectively. In Fig. 12 further results on *Screws* (real) are displayed. Here, in particular, the difference of *OIS*,

	<i>Screws</i> (generated)		<i>D2S</i>	
	<i>AAIS</i>	<i>OIS</i>	<i>AAIS</i>	<i>OIS</i>
Num GT	3121		16630	
Mean IoU (all)	68.9%	73.8%	73.0%	78.5%
Mean IoU (>0)	70.2%	76.0%	74.3%	79.8%
NumFNIoU (@0.75)	1844	1233	5482	3547
NumClassOk	2990	2998	13287	13522

TABLE IV: **Mean IoU evaluations.** NumGT: Number of ground truth instances in test dataset. Mean IoU (all): mean over maximum IoU values achieved for all ground truth instances. Mean IoU (>0): mean over maximum IoU values achieved for all ground truth instances where maximum IoU > 0 . NumFNIoU (@0.75): number of ground truth instances, where maximum IoU < 0.75 . NumClassOk: Number of predictions that achieved the maximum IoU value and where the predicted class was correct. See text for interpretation

OIS box from mask (bfm), and *OIS or from mask (ofm)* is visualized. Moreover, Fig. 13 shows some more examples for *Pill Bags* trained only with 10 percent of the instance masks. For all datasets, the displayed images are from the test set and were not seen during training.

The results also contain failure cases. Typical failure cases for *OIS* result from inaccurate box predictions, e.g. the orientation (ϕ), the center (r, c), or semi-axes ($l1, l2$) are not predicted correctly.

In this section, we show how we calculate the orientation of a region as used in Section 4.2.

Consider a region R consisting of n pixels with row coordinates r_i and column coordinates c_i , $i = 1, \dots, n$. We denote the center of gravity by $g = (r_0, c_0)$:

$$(r_0, c_0) = \frac{1}{n} \sum_{i=1}^n (r_i, c_i)$$

Further, the second moments of R , M_{ij} are given by:

$$M_{ij} = \sum_{(r,c) \in R} (r_0 - r)^i (c_0 - c)^j$$

We calculate the orientation ϕ of R by fitting an ellipse to the region that has the same aspect ratio and orientation and get:

$$\phi = -\frac{1}{2} \text{atan2}(2M_{11}, M_{02} - M_{20})$$

An example where this method to extract the orientation has benefits is given in Fig. 14. To obtain the bounding box with orientation ϕ calculated as above, we rotate the mask to be axis-aligned, get the axis-aligned bounding box, and rotate it back to have orientation ϕ .

As described in the main paper, we use two different architectures based on Mask RCNN [9] (M) and RetinaMask [8] (R). In contrast to the original implementation of RetinaMask we do not use the self-adjusting smooth L1-loss.

In comparison to [24], in the RPN we use branches similar to a RetinaNet with focal loss [18]. Therefore, we do not need box sampling during training. Moreover, we do not share weights between the fg/bg branch and the box branch and also do not share weights between different FPN-levels.

In the final mask prediction we use both a class specific and a class agnostic NMS. For both the IoU threshold can be set individually.

To make our results reproducible, we show all shared model settings for Mask RCNN with explanations in Table X and Table XI. In the following, we share the parameters that were changed for the application of our architecture on *D2S* and *Screws*. However, note that we do not claim that the given parameters are tuned optimally.

A. *D2S*

In comparison to *AAIS*, for *OIS* only the anchor aspect ratios and angles are adapted (*AAIS* has no anchor angles), see Table V. For RetinaMask [8] (R), we adapted the anchor aspect ratios for *OIS* such that in *AAIS* and *OIS* the same number of anchors is used.

parameter	<i>AAIS</i>	<i>OIS</i>
anchor parameter		
aspect ratios	(0.5, 1.0, 2.0) (M) (0.3, 0.6, 0.9, 1.11, 1.66, 3.33) (R)	(0.4, 0.7, 1.0) (M) (0.4, 0.9) (R)
angles	- (M, R)	$(-\frac{\pi}{3}, 0.0, \frac{\pi}{3})$ (M, R)
RPN parameter		
num convolutions	3 (M, R)	
max num post NMS	50 (R)	
RCNN head parameter (M)		
max num post NMS	28	
Mask head parameter		
num convs	2	

TABLE V: ***D2S* detailed model parameter settings.** Parameters for Mask RCNN (M) and RetinaMask (R) are shown. See text for further information

parameter	<i>AAIS</i>	<i>OIS</i>
backbone parameter		
backbone	SqueezeNet [12]	
dataset pretraining	OpenImages [15]	
freeze at	0 (no freeze)	
anchor parameter		
aspect ratios	(0.5, 1.0, 2.0)	(0.15, 0.35, 0.65, 1.0)
angles	-	$(-\frac{2\pi}{3}, -\frac{\pi}{3}, 0.0,$ $\frac{\pi}{3}, -\frac{2\pi}{3}, \pi)$
IgnoreDirection	-	false
RPN parameter		
min level	2	
max level	4	
max num pre NMS	400	
max num post NMS	512	
NMS IoU threshold	0.9	
conv dim	256	
final conv kernel size	3×3	
RPN training parameter		
box loss weight	2.0	
RCNN head parameter		
RoI min level	2	
RoI max level	4	
RoI canonical level	4	
NMS IoU threshold	1.0 (off)	
NMS IoU threshold agn	0.2	
max num pre NMS	512	
RCNN head training parameter		
batch size per img	512	
ratio num fg	0.9	
box angle weight	2.0	
Mask head parameter		
mask min score	0.4	

TABLE VI: ***Screws* detailed Mask RCNN model parameter settings.** See text for further information

B. *Screws*

In comparison to *D2S*, for *Screws*, the main differences are the lighter backbone and that IgnoreDirection is set to false, such that orientations in the range $(-\pi, \pi)$ are predicted. Accordingly, anchors for the full orientation range are used. We adapt the RPN parameters for high recall. All changed parameters for Mask RCNN are shown in Table VI.



Fig. 10: *D2S* results. (from left to right) input image, ground truth masks and generated ground truth oriented boxes, results based on axis-aligned boxes (AAIS), results based on oriented boxes (OIS) (best viewed digitally and with zoom)

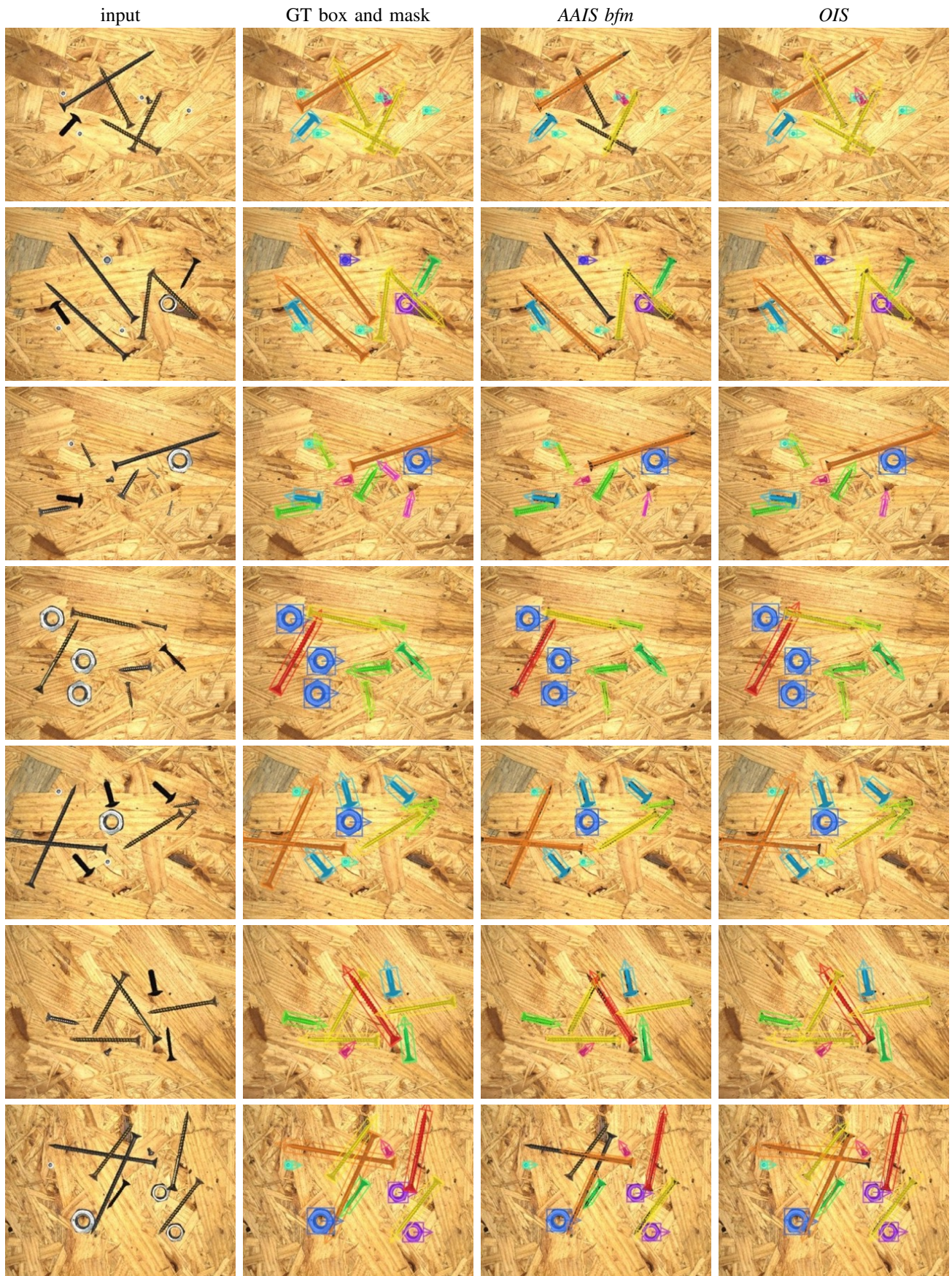


Fig. 11: **Screws (generated) results.** (best viewed digitally and with zoom)

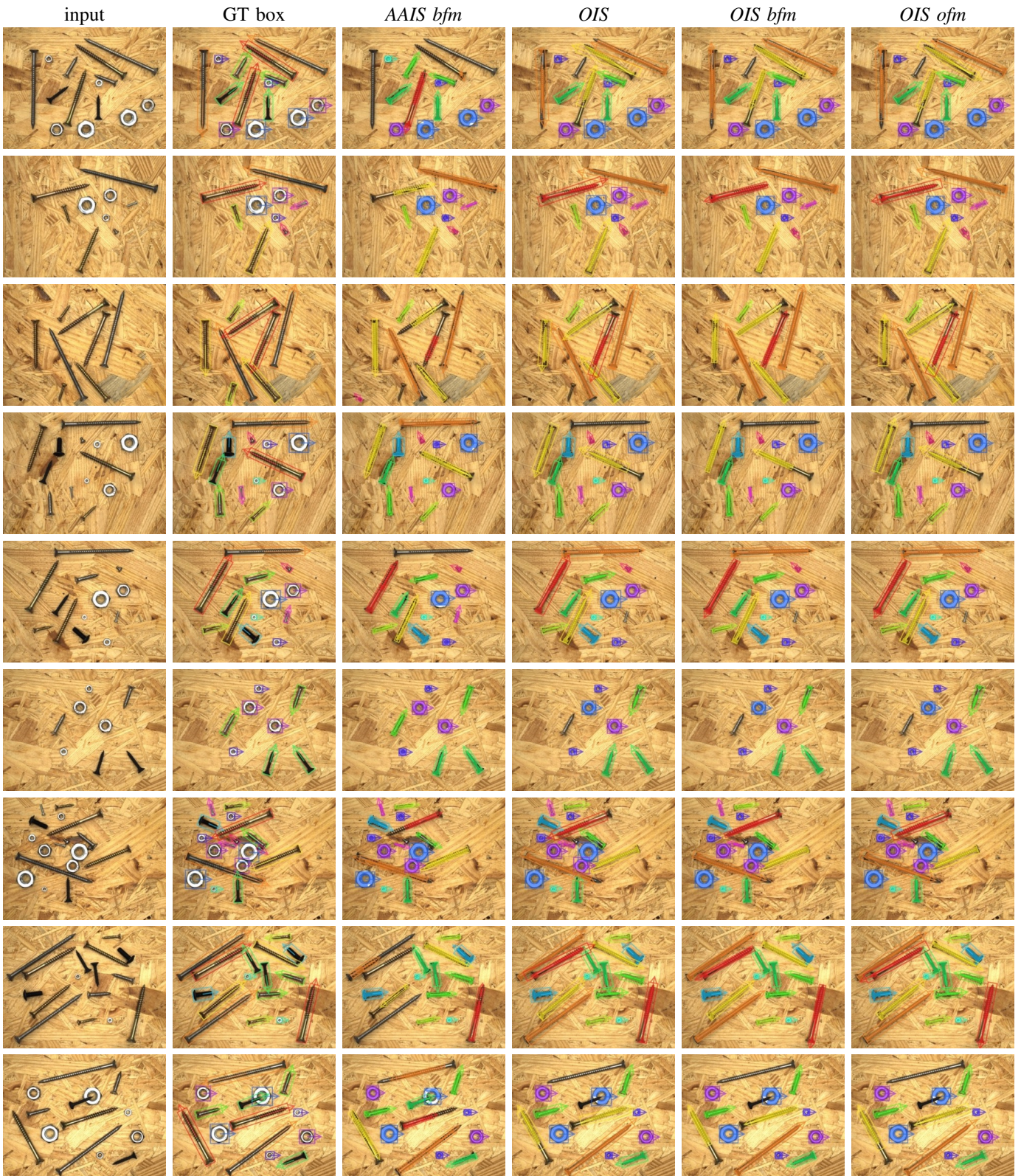


Fig. 12: **Screws (real) results.** For *OIS*, *OIS bfm*, and *OIS ofm* only the resulting box differs. (best viewed digitally and with zoom)

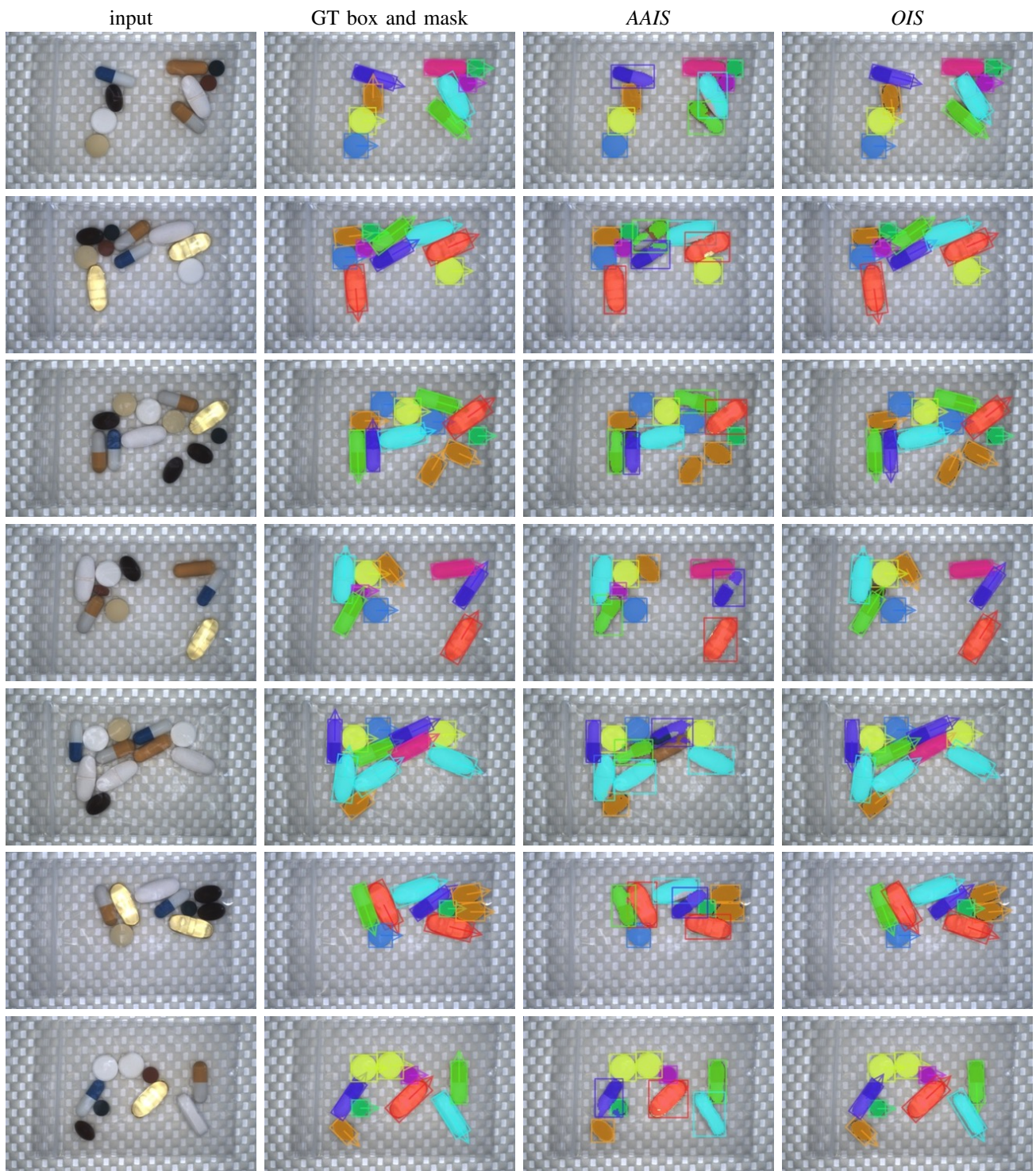


Fig. 13: *Pill Bags* results. Only 10 percent of the instance masks have been available during training. The shown images are from the test set (best viewed digitally and with zoom)

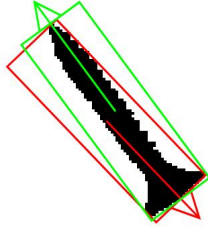


Fig. 14: **Example for orientation of region.** (black) underlying region R of a screw, (red) smallest oriented bounding box. (green) bounding box with orientation obtained from the region’s orientation. It points from the screws head to its tail and is therefore more consistent over different screw instances

parameter	<i>AAIS</i>	<i>OIS</i>
backbone parameter		
image size	512 x 320	
backbone	SqueezeNet [12]	
dataset pretraining	OpenImages [15]	
freeze at	0 (no freeze)	
anchor parameter		
num subscales	3	2
aspect ratios	(0.54, 1.00, 1.52, 2.31)	(0.38, 0.65, 1.00)
angles	-	(-0.80, 0.0, 0.75, 1.55)
RPN parameter		
min level	2	3
max level	4	
max num pre NMS	500	
max num post NMS	30	
NMS IoU threshold	0.14	0.1
NMS IoU threshold agn	0.25	0.1
final conv kernel size	3×3	
RPN training parameter		
fgNegThresh	0.4	
RCNN head parameter		
RoI min level	2	
RoI max level	4	
RoI canonical level	4	
NMS IoU threshold	1.0 (off)	
NMS IoU threshold agn	0.2	
max num pre NMS	512	
Mask head parameter		
num convs	2	
Mask head training parameter		
mask loss weight	2.0	

TABLE VII: *Pill Bags* detailed RetinaMask model parameter settings. See text for further information

C. Pill Bags

The detailed model parameter settings for RetinaMask trained on *Pill Bags* are shown in Table VII. The min and max level, anchor aspect ratios and angles (only for *OIS*) as well as the NMS IoU threshold and NMS IoU threshold agn were calculated automatically based on the distribution of bounding boxes in the training set. For the NMS IoU thresholds we require a minimum value of 0.1.

parameter	<i>Screws</i>	<i>D2S</i>	<i>Pill Bags</i>
momentum	0.9		
weight decay	1e-6		1e-5
initial learning rate	0.001		
lr strategy	step		
gamma (lr factor)	(0.1 0.01)		
steps	(30, 50)	(30, 40) (M) 25 (R)	(15, 30)
max epochs	60	50 (M) 40 (R)	35
batch size	2	4 (M) 2 (R)	2
warmup factor	0.33	0.1	0.33
warmup iterations	200	500	200

TABLE VIII: Solver parameters

All general solver settings are depicted in Table VIII. As for the model parameters, we do not claim that these parameters are optimal. However, we found that they lead to a stable training and we show them in such detail to make our results reproducible.

As we train all layers inside the heads and the FPN from scratch, we found that the training was diverging easily. This problem could be fixed by a dynamic loss weighting strategy as described in the following subsection.

D. Dynamic loss weights

Besides the backbone, all layers within the FPN, RPN, RCNN and mask branches are not pretrained but initialized randomly. Both the RPN branches as well as the RCNN heads are using features from the FPN. However, in the beginning of the training, the box deltas and classes that are predicted by the RCNN heads are mostly wrong and generate large losses. This results in large gradients that are not aligned with the gradients of the RPN. This leads to frequent divergence of the training.

Therefore, at the beginning of the training, when the RPN loss is still high, we reduce both the box loss weight and the class loss weight to low initial values (ilw_{box} and ilw_{class}). During training, we dynamically increase those loss weights linearly to the final box loss weight flw_{box} and the final class loss weight flw_{cls} . This is done over n_{dlw} iterations: whenever the running average RPN loss \bar{l}_{RPN} falls below the current RPN loss threshold Tl_{RPN} , the box and class loss weights are increased and Tl_{RPN} is multiplied by a factor $\delta Tl_{RPN} < 1$.

More formally: Initialize the current loss weights for box $lw_{box} = ilw_{box}$ and class $lw_{cls} = ilw_{cls}$. Initialize the current RPN loss threshold $Tl_{RPN} = iTl_{RPN}$. Initialize the current iteration $i_{dlw} = 0$. Let \bar{l}_{RPN} be the total RPN loss averaged over the last 10 iterations. Let δlw_{box} and δlw_{cls} be the stepsizes for the box and class loss weights, respectively:

$$\delta lw_{box} = \frac{flw_{box} - ilw_{box}}{n_{dlw}}$$

$$\delta lw_{cls} = \frac{flw_{cls} - ilw_{cls}}{n_{dlw}}$$

parameter	<i>Screws</i>	<i>D2S</i>
ilw_{box}	0.01	
ilw_{cls}	0.01	
flw_{box}	1.0	
flw_{cls}	1.0	2.0
iTl_{RPN}	0.5	
n_{dlw}	50	

TABLE IX: **Dynamic loss weight parameters**

Now always if $\bar{l}_{RPN} < Tl_{RPN}$ and $i_{dlw} < n_{dlw}$, we update:

$$\begin{aligned}
 lw_{box} &\leftarrow lw_{box} + \delta lw_{box} \\
 lw_{cls} &\leftarrow lw_{cls} + \delta lw_{cls} \\
 Tl_{RPN} &\leftarrow Tl_{RPN} \cdot \delta Tl_{RPN} \\
 i_{dlw} &\leftarrow i_{dlw} + 1
 \end{aligned}$$

For our experiments we use the parameters as shown in Table IX. They remain unchanged for *AAIS* and *OIS*. The dynamic loss weight strategy is only used for Mask RCNN [9], but not for RetinaMask [8].

parameter	default value	explanation
backbone parameter		
image size	512×384	input image dimensions (w, h)
backbone	ResNet50 [10]	backbone classifier network
dataset pretraining	ImageNet [4]	dataset for pretraining
freeze at	3	The first n layers of the backbone are frozen
RPN parameter		
min level	3	minimum used FPN level
max level	5	maximum used FPN level
max num pre NMS	512	maximum number of boxes before NMS is applied (per FPN level)
max num post NMS	256	maximum number of boxes after NMS was applied (total)
NMS IoU threshold	0.8	IoU threshold for NMS
min side length	1.0	minimum side length of output boxes
num convolutions	4	number of convolutions in RPN branches
conv dim	128	number of kernels for the intermediate convolutions of the RPN
final conv kernel size	1×1	kernel size of final convolution in RPN branches
min score	0.05	minimal score of output boxes (only inference)
anchor parameter		
num subscales	3	number of subscales/octaves for each anchor
aspect ratios	(0.5, 1.0, 2.0)	aspect ratios of anchors
angles	$(-\frac{2\pi}{3}, 0.0, \frac{2\pi}{3})$	orientations of anchors (only for <i>OIS</i>)
IgnoreDirection	true	See paper, only for oriented boxes
RPN training parameter		
fgPosThresh	0.5	positive threshold for anchor assignment
fgNegThresh	0.3	negative threshold for anchor assignment
swb2bg	false	if true, anchors below fgNegThresh are always assigned to background
fg/bg loss weight	1.0	loss weight for fg/bg branch
box loss weight	1.0	loss weight for box branch
box center weight	2.0	loss factor for (r,c) prediction
box dim weight	1.0	loss factor for $(w, h)/(l1, l2)$ prediction
box angle weight	1.0	loss factor for ϕ prediction
focal loss gamma	2.0	gamma in RPN focal loss
focal loss beta	0.11	beta in RPN focal loss

TABLE X: Model parameters with explanations part 1

parameter	default value	explanation
RCNN head parameter		
RoI min level*	3	minimum FPN level for RoI pooling
RoI max level*	5	maximum FPN level for RoI pooling
RoI canonical scale*	224	anchors of canonical scale are distributed to the canonical level see [24]
RoI canonical level*	5	
RoI pool mode*	roi_pool	In this work, we only use the original RoI pooling (no RoIAlign)
RoI grid size (M)	(7, 7)	RoI pooling grid size (w, h) for RCNN head
MLP head dim (M)	256	dim of intermediate fc layer of RCNN head MLP
NMS IoU threshold	0.3	class specific IoU threshold (only inference)
NMS IoU threshold agn	0.3	class agnostic IoU threshold (only inference)
max num pre NMS	256	maximum number of boxes before NMS is applied (only inference)
max num post NMS	30	maximum number of boxes after NMS was applied (only inference)
min score	0.5	minimal score of output boxes (only inference)
RCNN head training parameter		
fgPosThresh	0.7	positive threshold for box assignment
fgNegThresh	0.5	negative threshold for box assignment
swb2bg	true	if true, boxes below fgNegThresh are always assigned to background
batch size per img	256	maximum number of samples per image
ratio num fg	0.75	Ratio of fg/bg samples in batch
class loss weight	dlw	we use a dynamic loss weight strategy
box loss weight	dlw	we use a dynamic loss weight strategy
box center weight	2.0	loss factor for (r,c) prediction
box dim weight	1.0	loss factor for $(w, h)/(l1, l2)$ prediction
box angle weight	1.0	loss factor for ϕ prediction
Mask head parameter		
num convs	4	number of convolutions in mask head
conv dim	128	number of kernels in intermediate convs
RoI grid size	(14, 14)	RoI pooling output size (w, h) for mask head
Mask final grid size	(28, 28)	mask output and target size (w, h)
mask min score	0.5	minimum score for mask prediction (only inf.)
Mask head training parameter		
fgPosThresh	0.7	positive threshold for final box assignment
fgNegThresh	0.6	negative threshold for final box assignment
swb2bg	true	if true, boxes below fgNegThresh are always assigned to background
mask loss weight	1.0	weight of mask branch loss

TABLE XI: Model parameters with explanations part 2. (*) Parameters are shared between RCNN and mask heads